The 9th European Congress on Computational Methods in Applied Sciences and Engineering
ECCOMAS Congress 2024
3–7 June 2024, Lisboa, Portugal

A STATISTICAL-BASED HEMODYNAMICS STUDY FOR AORTIC AND PULMONARY DISTRICTS

MARILENA MAZZOLI[1,2], BENIGNO M. FANNI[1], KATIA CAPELLINI[1], LAMIA AIT-ALI[3,4], ANGELO MONTELEONE[4] AND SIMONA CELI[1]

[1] BioCardioLab, Bioengineering Unit
Fondazione Toscana Gabriele Monasterio, Massa, Italy
email: mmazzoli@ftgm.it, bmfanni@ftgm.it, kcapellini@ftgm.it, s.celi@ftgm.it

[2] Department of Information Engineering
University of Pisa, Pisa, Italy

[3] Institute of Clinical Physiology
CNR, Massa, Italy
email: lamia.ait-ali@cnr.it

[4] Department of Radiology
Fondazione Toscana Gabriele Monasterio, Massa, Italy
email: amonteleone@ftgm.it

Key words: Statistical Shape Model, Non-Rigid Registration, Computational Fluid Dynamics

1 INTRODUCTION

Over the past few years, there has been an increase of clinical interest aimed at looking for correlations between morphology, extracted through Statistical Shape Models (SSMs), and hemodynamic features, derived from Computational Fluid Dynamic (CFD) simulations, in cardiovascular diseases [1]. Statistical Shape Models are well-established tools for assessing the variability of vascular geometries. Starting from a heterogeneous population, SSMs can provide useful biomarker information in terms of geometrical features (e.g. size, curvature, orientation) [2]. SSMs are based on a non-rigid registration process, which can be challenging to perform with complex anatomies, coupled with a dimensionality reduction step, typically achieved through Principal Component Analysis (PCA). Thoracic aorta diseases can present a particularly complex morphological scenario, and several studies in literature have explored the connection between vessel geometry and hemodynamics [3]. These studies mainly focused on a patient-specific investigation, with no statistical analyses. Due to the complex shapes involved, when a statistical perspective is employed, the supra-aortic vessels are excluded [4] or modeled in an idealised manner [5]. This is also true when the hemodynamic descriptors are derived from CFD simulations [6]. In the context of the pulmonary artery (PA), Tetralogy of Fallot (ToF) represents a complex case of cardiovascular disease, where geometries are subject to significant variations. Despite the overall geometry presents a simplified scenario, the associated Y-shape varies considerably among patients. Furthermore, since this disease predominantly affects paediatric patients, the complexity of studying these morphologies is further increased by the surgeries they have undergone. Capuano and colleagues [7] studied the flow split by applying

an SSM to five healthy patients. In [8], the geometric variability and flow distribution in the pulmonary arteries of seven ToF patients were studied with respect to blood flow characteristics. More recently, the differences in blood flow dynamics between healthy adults and those who have undergone repair for ToF were also investigated [9].
The aim of this work is to present a fully automated pipeline able to correlate morphology and hemodynamic results for two complex cardiovascular districts: thoracic aortas affected by aneurysms and pulmonary arteries with Tetralogy of Fallot. The framework combines the ability of SSMs to quantify shape complexity and to generate new realistic geometries, to hemodynamic results from CFD simulations. Finally, a correlation study between the morphological and hemodynamic features, derived from SSMs and CFD simulations respectively, is presented.

2 MATERIALS AND METHODS

2.1 Image processing

A total of 50 thoracic aortas from CT and 40 pulmonary arteries from MRI were considered. The dataset of thoracic aortas included both healthy and aneurysmatic cases; while all the pulmonary arteries were affected by Tetralogy of Fallot. Table 1 reports the clinical data for both datasets.

Table 1: Population demographic and clinical data.

District	**Dataset**	**Image technique**	**Age** (years)	**Sex** (females/males)
Aorta	50	CT	65.7 ± 13	18/32
Pulmonary	40	MR	22 ± 10	22/18

The images were processed with a semi-automatic segmentation approach in 3D-Slicer [10] using a region-growing algorithm to extract the 3D virtual geometries. Segmented anatomies were further refined using the open source software Meshmixer (Autodesk Inc., USA) to improve surface quality.

2.2 Statistical Shape Models

In Scarpolini et al. [11] our non-rigid registration algorithm able to include the supra-aortic vessels in the analysis of complex morphology of thoracic aortas was presented. Briefly, the key concept of a non-rigid registration process is to deform a source surface mesh $\mathcal{M}_s$ into a target surface mesh $\mathcal{M}_t$ [12]. This goal was obtained with the minimization of the objective function $\phi(\mathcal{M}_s, \mathcal{M}_t)$, described in Eq.1. This includes both the distance between the two whole surfaces $d(\mathcal{M}_s, \mathcal{M}_t)$ and the distance between pairs of open boundaries $\sum_{j=1}^{n} \alpha_j d(B_s^j, B_t^j)$, where n is the number of open boundaries and B_s^j and B_t^j are the set of points on the j-th open boundary of the source and target mesh, respectively.

$$\phi(\mathcal{M}_s, \mathcal{M}_t) = d(\mathcal{M}_s, \mathcal{M}_t) + \sum_{j=1}^{n} \alpha_j d(B_s^j, B_t^j) \tag{1}$$

This latter term acted as landmarks to achieve the correct registration of the supra-aortic

branches ($n = 5$) and, when the code was adapted to the pulmonary cases, the summation of the latter term in Eq.1 was reduced to $n = 3$ as there are only three open boundaries in the pulmonary arteries. The update rule for the minimization problem used a modified second-order gradient descent approach. To enhance registration performances, the registration process was iteratively applied four times using a multi-scale strategy with varying mesh resolutions. This multi-scale non-rigid registration algorithm $\mathfrak{R}(\mathcal{M}_s, \mathcal{M}_t)$ was applied between the source $\mathcal{M}_s$ template geometry and each model of the dataset $\mathcal{M}_t^i$ ($i = 1, ..., M$ with M=50/40 as the total number of aortas and PAs, respectively). This allowed to represent each of all the 3D models of the starting dataset as shape $\mathbf{s}$, i.e. as a vector were the coordinates of the k-points are concatenated:

$$\mathbf{s} = (x_1, y_1, z_1, ..., x_k, y_k, z_k)^T \tag{2}$$

This process produced the *shape* dataset, characterised by isotopological surface meshes, meaning all meshes had three main features: (i) same number of k-points; (ii) same connectivity and; (iii) point-to-point correspondence. To evaluate registration performances, the Chamfer and Hausdorff distances were measured between the initial and the *shape* datasets for each sample. Lastly, to create the SSM, it was necessary to reduce the dimensionality of the dataset. Principal Component Analysis is one of the most commonly used tools for this purpose. It is a statistical procedure that allows summarizing the information in large data tables with minimal information loss. PCA performs eigendecomposition of the covariance matrix S of the *shape* dataset as follows:

$$S = \frac{1}{M-1} \sum_{i=1}^{M} (\mathbf{s}_i - \bar{\mathbf{s}})(\mathbf{s}_i - \bar{\mathbf{s}}) \tag{3}$$

Then it extracts the $m = \min((M-1), 3k)$ principal *modes* of variation (eigenvectors ϕ_i) and their associated variances (eigenvalues λ_i). These *modes* are uncorrelated and ordered by decreasing values of variance ($\lambda_1 \geq ... \geq \lambda_m$). For the purposes of dimensionality reduction, the number of *modes* was reduced to the first $m' = 16$ ones, as the percentage of their cumulated variance is ∼98% and ∼97% for the thoracic aortas and PAs, respectively (Fig. 1). These percentages indicate that the mesh reconstruction, which involves a linear combination of the anatomical *modes* that deform the average mesh, can be achieved without significant information loss. At this point, new realistic shapes can be generated by varying the coefficients ω_i from a Gaussian distribution, of the linear combinations:

$$\mathbf{s} = \bar{\mathbf{s}} + \sum_i \omega_i \phi_i \tag{4}$$

2.3 CFD simulations

Concerning the aortic district, by varying *mode* 0, we observed a variation from a healthy to a complete aneurysmatic shape and this is due to the fact that this *mode* accounts for most of the variability within the dataset (∼35%). CFD simulations were carried out on five new shapes, generated by varying the coefficients ω_i between ±2 standard deviation (SD) of this first *mode* ($\sqrt{\lambda_1}$), with intermediate steps of 1.
In the PAs cases, however, it is the study of the flow split at the bifurcation which is of clinical interest, so we focused on the variation of *mode* 4. The volumetric meshes were generated with

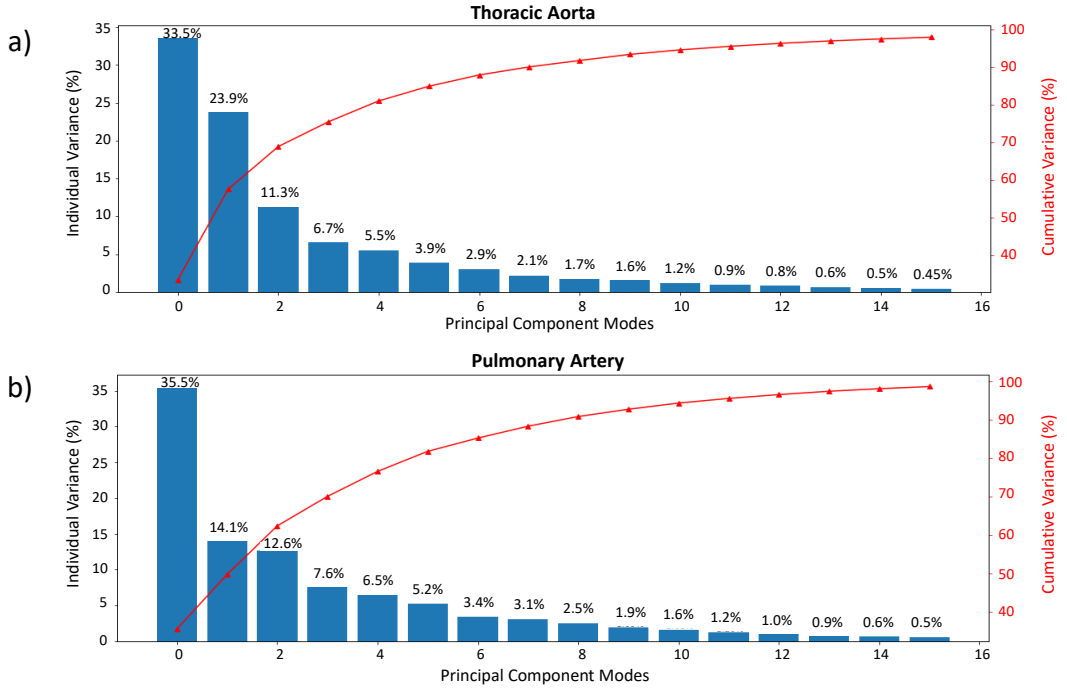

Figure 1: Individual and Cumulative variance of the first 16 *modes* for both the thoracic aorta (a) and the pulmonary arteries (b). The percentage of the cumulated variance is ∼98% for the thoracic aortas and ∼97% for the PAs.

an automatic in-house script which prepares the superficial mesh as a multiblock model with wall, caps and extensions and generates the volumetric mesh in ANSA BETA CAE. The meshes were characterized by an average element edge size of 1 mm and an imposed target skewness of 0.45. The numerical simulations were conducted using $Ansys^{TM}$ $Fluent^{TM}$, where the 3D incompressible Navier-Stokes equations were solved numerically in their discrete form using the finite volume method for blood flow simulation. Blood was modeled as an incompressible, Newtonian, and laminar fluid with a constant density of 1060 kg/m^3 and a viscosity of 3.5 $10^{-3} Pa \cdot s$. The arterial wall was assumed to be rigid with no-slip conditions. Three cardiac cycles of 0.8 seconds each were simulated, and results from only the last cycle were considered. Figure 2 depicts the boundary conditions applied for each district. Since the simulations had to be run on the same mesh resulting from the PCA statistical atlas deformed between ±2 SD of *mode* 0 and of *mode* 4, fixed ideal flows were applied at the inlets: the ascending aorta [13], and the main pulmonary artery (MPA) [14]. This resulted in a variable inlet velocity, depending on the inlet area of each mesh itself.

For the thoracic aorta, a three element Windkessel model was applied at the four outlets: the three supra-aortic branches and the descending aorta. The associated RCR model is composed of a proximal resistance R_P, in series with a parallel made of a distal resistance R_D and a capacitance C [15]. For the calculation of the Windkessel parameters, the process described in Xiao et al. [16] was applied. The associated pressure was derived from the following ordinary

differential equation:

$$P(t) + R_D C \frac{dP(t)}{dt} = R_P + R_D Q(t) + R_P R_D C \frac{dQ(t)}{dt} + P_D(t) + R_P C \frac{dP_D(t)}{dt} \tag{5}$$

For the PAs a constant pressure was applied at the two outlets corresponding to the left and right pulmonary artery (LPA and RPA, respectively) as described in Fanni et al. [17].

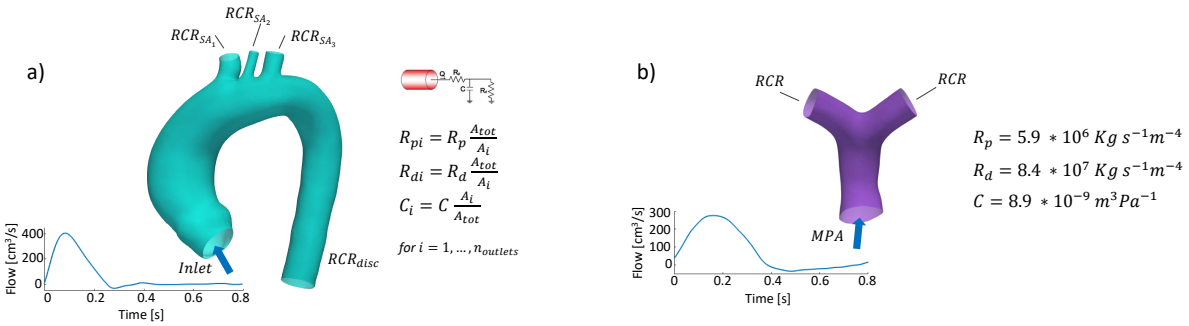

Figure 2: CFD simulation setup for a) the thoracic aorta and b) the pulmonary arteries with an ideal flow at the inlet and the RCR lumped model at the outlets.

2.4 Correlation Analysis

In order to asses the effects of the morphology on the hemodynamics, the wall shear stress (WSS)-based descriptors were evaluated for the aortic vessel. In particular, the Time Averaged Wall Shear Stress (TAWSS), the Oscillatory Shear Index (OSI), and the Endothelial Cell Activation Potential (ECAP) were calculated as follows:

$$TAWSS = \frac{1}{T} \int_0^T |WSS(t)| \cdot dt \tag{6}$$

$$OSI = 0.5 \left(1 - \frac{\left| \int_0^T WSS(t) \cdot dt \right|}{\int_0^T |WSS(t)| \cdot dt} \right) \tag{7}$$

$$ECAP = \frac{OSI}{TAWSS} \tag{8}$$

The TAWSS represents the average WSS magnitude over the total time of a cardiac cycle (T); the OSI quantifies the change in direction and magnitude of WSS; while the ECAP is the

ratio between OSI and TAWSS and characterizes the degree of thrombogenic susceptibility of the vessel wall. We focused the investigation on the ascending aortic portion, as this is the area characterised by the aneurysmatic dilation. The aneurysms was selected on the mesh at +2 SD, as this is where the aneurysm is most evident. The point-to-point correspondence achieved with the SSM allowed us to apply this selection to all the other four meshes simply by using point identifiers. Traditional bivariate correlation analysis (Pearson correlation coefficient r and p-value p were evaluated) was then employed to evaluate these correlations.
In the PAs cases, we focused our attention on the flow split at the bifurcation, as this is the parameter of greatest clinical interest. This flow split was evaluated in relation to the geometric changes.

3 RESULTS

3.1 Statistical Shape Models

Figure 3 depicts the results of the non-rigid registration process for both the aorta with the supra-aortic vessels (Fig. 3a) and the pulmonary arteries (Fig. 3b). As we can observe, during the registration process, as coarser details were captured, the resolution increases to cope with finer details. Similarly, the registration process for the pulmonary arteries was successful,

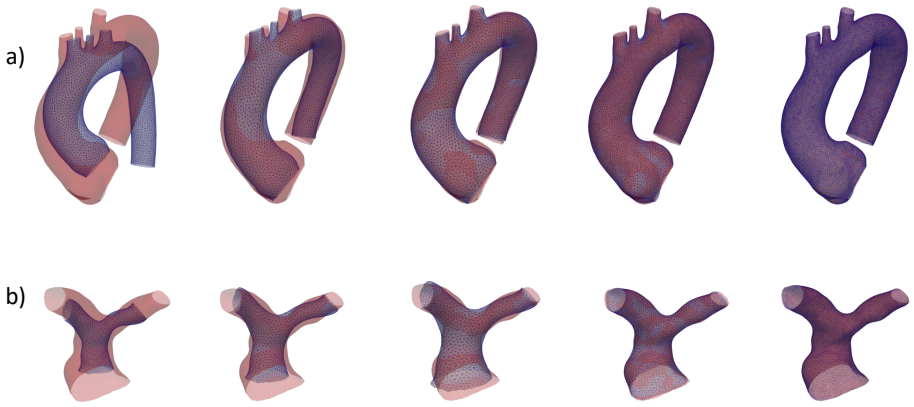

Figure 3: Examples of non rigid registration results for a) thoracic aorta and b) pulmonary artery. The template geometry (blue) is deformed in the target mesh (red) with changes in resolution during the process.

despite the geometries were very peculiar and different from each other (Fig. 3b). Evaluations using Chamfer and Hausdorff distances between the registered shapes and the original targets showed a maximum error of 0.5 mm, consistent with the average edge length of each surface mesh. Regarding dimensionality reduction, we retained the first 16 *modes* as they accounted for almost 98 and 97% of the total variability in the dataset (aorta and PA, respectively). This ensured minimal information loss when reconstructing and generating new geometries. As expected, since the aorta dataset was made of both healthy and aneurysmatic patients, the change of *mode* 0 from -2 to +2 standard deviation, resulted in a geometry-change from a healthy to a completely aneurysmatic shape (Fig. 4a). A variation in the size and curvature of LPA and

RPA can be observed in the variation of *mode* 4 (Fig. 4b).

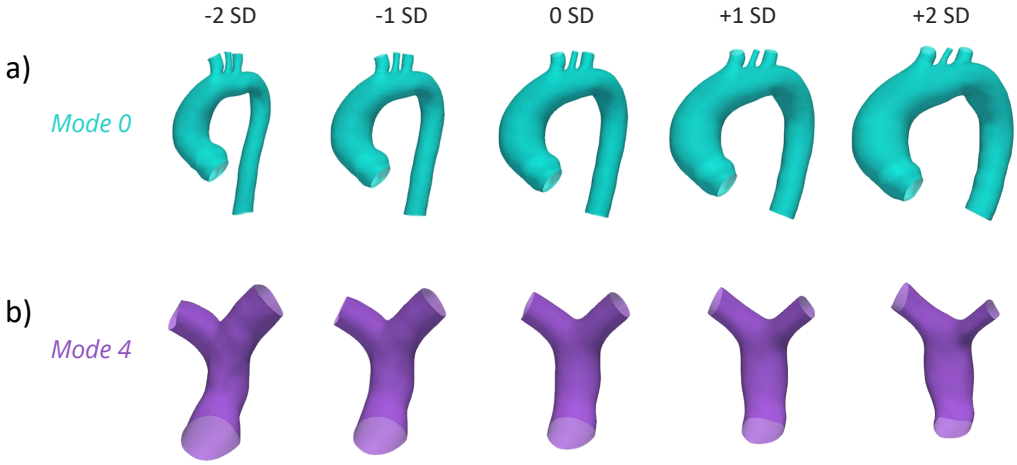

Figure 4: New generated shapes for a) the thoracic aorta and b) the pulmonary arteries by varying *mode* 0 and *mode* 4 from -2 to +2 standard deviation, respectively.

3.2 CFD Simulations and Correlation Analysis

Figure 5 shows the results of the CFD simulations performed on the variation of *mode* 0 for the thoracic aorta. In particular, we can observe that low WSS values (< 1 Pa) were associated with aneurysmatic shapes, whereas smaller shapes (-2 SD) exhibited higher WSS values (Fig. 5a). A similar negative correlation was observed for TAWSS values (Fig. 5b). Conversely, OSI and ECAP showed the opposite trend: as the aneurysm volume increased, the values of these indices also increased (Fig. 5c,d). Significant r values over 95% with p values below 0.05% were found for WSS ($r = -0.97\%$ $p = 0.007$), TAWSS ($r = -0.96\%$ $p = 0.009$) and ECAP ($r = 0.96\%$ $p = 0.001$).

Analyzing the outcomes of the PAs, from the third column of Figure 6, we can see how the flow split at the different bifurcations is influenced by the geometry of the vessel itself. In particular as the area of the LPA decreases, the flow increases in the RPA, as does its area. In the second column of Figure 6, velocity streamlines and velocity through plane at the systolic peak are reported for the PAs.

4 DISCUSSION AND CONCLUSIONS

In this work, we evaluated the influence of vascular geometry on the hemodynamics of two vessels affected by cardiovascular diseases: aneurysmatic aortas and pulmonary arteries affected by Tetralogy of Fallot. In fact, when dealing with these two pathologies, the vascular hemodynamics is highly variable and it is deeply affected by different geometrical vascular features. Since this geometrical dependence is pivotal for a deeper understanding of these pathological vascular hemodynamics, an automated pipeline was developed to extract vessels' morphologi-

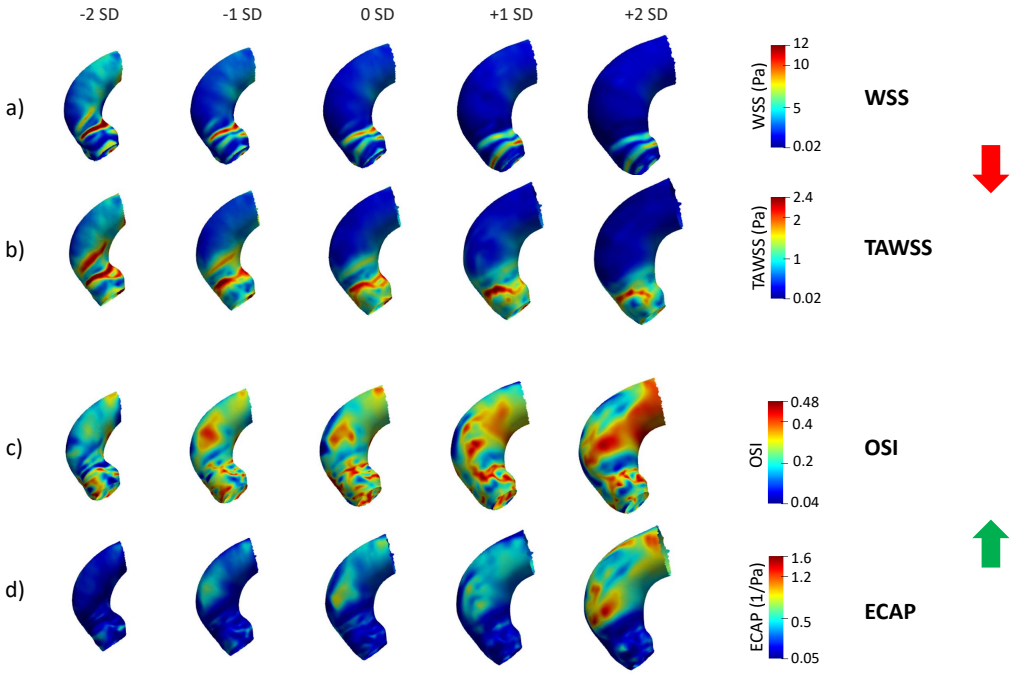

Figure 5: Correlation results between the variation of the aneurysm from -2 to +2 SD of *mode* 0 and hemodynamic parameters. Negative correlations with a) WSS and b) TAWSS; while positive correlations with c) OSI and d) ECAP.

cal parameters via SSM and fluid dynamic indexes via CFD simulations. Finally, the results obtained from this procedure were correlated to understand how and whether geometry affects hemodynamics. First of all, we assessed the capability of our non-rigid registration algorithm, initially developed for the thoracic aorta [11], to effectively handle another great vessel with a different pathology: the pulmonary artery affected by Tetralogy of Fallot. The code was adapted to manage the intrinsic differences of the pulmonary artery with respect to the aorta, obtaining optimal registration outcomes with negligible errors. In addition, we also tested the potentiality of these generated SSMs to create new realistic geometries, from healthy to pathological vessels, on which it is possible to carry out CFD simulations for hemodynamics analysis. Indeed, the CFD results of these new synthetic data could be of clinical support for preventive diagnosis in real patients who have similar geometry to those tested. In the case of patients with aortic aneurysm, it was possible to delineate the relationship between shear forces along the vascular wall and morphological parameters, particularly the increase of volume observed in the five thoracic aorta geometries. Significant correlations between the variation in size and the hemodynamic parameters were discovered, which may be important biomarkers for the pathological processes. Specifically, we observed low WSS and TAWSS values in the aneurysmatic area (negative correlation Fig. 5a,b), along with high OSI and ECAP values (positive correlation Fig. 5c,d). These results are statistically significant, as indicated by the high Pearson coefficient and a significant $p-value$ of less than 0.05%. The only exception is the OSI value ($r = 0.8\%$ $p = 0.12$), which has a higher $p-value$, likely due to the limited dataset and small sample size.

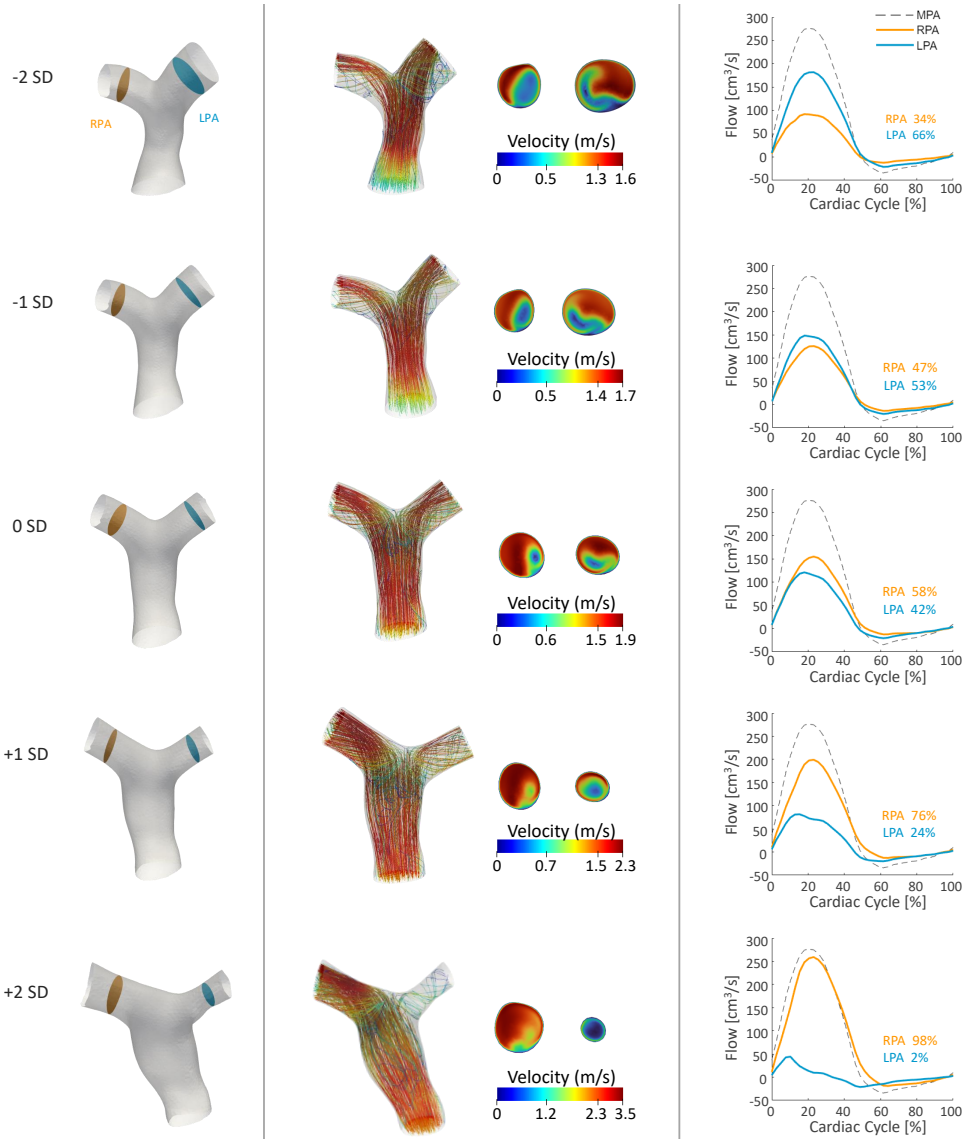

Figure 6: In the first column the five generated geometries from the variation of *mode* 4 from -2 to +2 SD. In the second column velocity streamlines and velocity through plane. In the third column the percentages of flow splits are reported: as the LPA area decreases the flow increases in the RPA, as does its area.

Our findings for the thoracic aorta are consistent with those reported in the literature ([18], [19], [20], [21], [22], [23], [24]). It is also worth noting that very high (WSS and TAWSS) and low (OSI and ECAP) hemodynamic values were observed in the sinotubular junctions, which could be due to the different curvature of these regions. Regarding the pulmonary arteries affected by Tetralogy of Fallot, the morphology was investigated in relation to the flow split of the bifurcations. In particular, the *mode* 4 was chosen because this highlighted a variation in the size and curvature of the two bifurcations (LPA and RPA). The results showed that there was an increase of the flow in the RPA, as the LPA area decreases.

Future developments could investigate variations of other modes, linked to different morphologies. Many other parameters could also be investigate such as tortuosity, ratio of ascending to descending aorta diameter and so on. In the context of the SSM framework, future efforts should focus on further automating the entire processing pipeline. Ideally, a newly scanned patient's shape would be instantly added to a local or cloud-based SSM database, enabling immediate comparison of the patient with a selected population. This would allow for the direct calculation of shape biomarker values, abnormality scores, or clustering visualizations, which could be seamlessly integrated into the diagnostic process. One of the main limitations of this study is the relatively small patient sample size. In the future, incorporating additional geometries, including those from patients with new pathologies, could enhance and update the SSM. Additionally, it would be beneficial to include more clinically relevant functional or outcome parameters to identify clusters of patients with high or low risk.

In conclusion, the methods and tools presented for analyzing shape and function demonstrate significant potential to enhance our understanding of complex structural diseases. This could lead to the development of improved diagnostic and risk stratification strategies, and possibly new surgical approaches.

REFERENCES

[1] Rodero, C., Strocchi, M., Marciniak, M., Longobardi, S., Whitaker, J., O'Neill, M.D., Gillette, K., Augustin, C., Plank, G., Vigmond, E.J. and Lamata, P., 2021. Linking statistical shape models and simulated function in the healthy adult human heart. PLoS computational biology, 17(4), p.e1008851.

[2] Sophocleous, F., Biffi, B., Milano, E.G., Bruse, J., Caputo, M., Rajakaruna, C., Schievano, S., Emanueli, C., Bucciarelli-Ducci, C. and Biglino, G., 2019. Aortic morphological variability in patients with bicuspid aortic valve and aortic coarctation. European Journal of Cardio-Thoracic Surgery, 55(4), pp.704-713.

[3] Capellini, K., Vignali, E., Costa, E., Gasparotti, E., Biancolini, M.E., Landini, L., Positano, V. and Celi, S., 2018. Computational fluid dynamic study for aTAA hemodynamics: an integrated image-based and radial basis functions mesh morphing approach. Journal of biomechanical engineering, 140(11), p.111007.

[4] Bruse, J.L., Khushnood, A., McLeod, K., Biglino, G., Sermesant, M., Pennec, X., Taylor, A.M., Hsia, T.Y., Schievano, S., Khambadkone, S. and De Leval, M., 2017. How successful is successful? Aortic arch shape after successful aortic coarctation repair correlates with left ventricular function. The Journal of thoracic and cardiovascular surgery, 153(2), pp.418-427.

[5] Catalano, C., Agnese, V., Gentile, G., Raffa, G.M., Pilato, M. and Pasta, S., 2021. Atlas-based evaluation of hemodynamic in ascending thoracic aortic aneurysms. Applied Sciences, 12(1), p.394.

[6] Pajaziti, E., Montalt-Tordera, J., Capelli, C., Sivera, R., Sauvage, E., Quail, M., Schievano, S. and Muthurangu, V., 2023. Shape-driven deep neural networks for fast acquisition of aortic 3D pressure and velocity flow fields. PLoS Computational Biology, 19(4), p.e1011055.

[7] Capuano, F., Loke, Y.H. and Balaras, E., 2019. Blood flow dynamics at the pulmonary artery bifurcation. Fluids, 4(4), p.190.

[8] Boumpouli, M., Sauvage, E.L., Capelli, C., Schievano, S. and Kazakidi, A., 2021. Characterization of flow dynamics in the pulmonary bifurcation of patients with repaired tetralogy of fallot: A computational approach. Frontiers in Cardiovascular Medicine, 8, p.703717.

[9] Boumpouli, M., Black, S.M. and Kazakidi, A., 2024. Computational analysis of blood flow in healthy pulmonary arteries in comparison to repaired Tetralogy of Fallot results: a small cohort study. Fluids, 9(4), p.85.

[10] Kikinis, R., Pieper, S.D. and Vosburgh, K.G., 2013. 3D Slicer: a platform for subject-specific image analysis, visualization, and clinical support. In Intraoperative imaging and image-guided therapy (pp. 277-289). New York, NY: Springer New York.

[11] Scarpolini, M.A., Mazzoli, M. and Celi, S., 2023. Enabling supra-aortic vessels inclusion in statistical shape models of the aorta: a novel non-rigid registration method. Frontiers in Physiology, 14, p.1211461.

[12] Nicolet, B., Jacobson, A. and Jakob, W., 2021. Large steps in inverse rendering of geometry. ACM Transactions on Graphics (TOG), 40(6), pp.1-13.

[13] Capellini, K., Gasparotti, E., Cella, U., Costa, E., Fanni, B.M., Groth, C., Porziani, S., Biancolini, M.E. and Celi, S., 2021. A novel formulation for the study of the ascending aortic fluid dynamics with in vivo data. Medical Engineering & Physics, 91, pp.68-78.

[14] Fanni, B.M., Pizzuto, A., Santoro, G. and Celi, S., 2022. Introduction of a novel image-based and non-invasive method for the estimation of local elastic properties of great vessels. Electronics, 11(13), p.2055.

[15] Vignon-Clementel, I.E., Figueroa, C.A., Jansen, K.E. and Taylor, C.A., 2010. Outflow boundary conditions for 3D simulations of non-periodic blood flow and pressure fields in deformable arteries. Computer methods in biomechanics and biomedical engineering, 13(5), pp.625-640.

[16] Xiao, N., Alastruey, J. and Alberto Figueroa, C., 2014. A systematic comparison between 1-D and 3-D hemodynamics in compliant arterial models. International journal for numerical methods in biomedical engineering, 30(2), pp.204-231.

[17] Fanni, B.M., Gasparotti, E., Vignali, E., Capelli, C., Positano, V. and Celi, S., 2023. An integrated in-vitro and in-silico workflow to study the pulmonary bifurcation hemodynamics. Computers & Fluids, 260, p.105912.

[18] Natsume, K., Shiiya, N., Takehara, Y., Sugiyama, M., Satoh, H., Yamashita, K. and Washiyama, N., 2017. Characterizing saccular aortic arch aneurysms from the geometry-flow dynamics relationship. The Journal of thoracic and cardiovascular surgery, 153(6), pp.1413-1420.

[19] Mousavi, S.J., Jayendiran, R., Farzaneh, S., Campisi, S., Viallon, M., Croisille, P. and Avril, S., 2021. Coupling hemodynamics with mechanobiology in patient-specific computational models of ascending thoracic aortic aneurysms. Computer Methods and Programs in Biomedicine, 205, p.106107.

[20] Horvat, N., Zambrano, B., Baek, S. and Karšaj, I., 2017. Numerical modeling of fluid solid growth in abdominal aortic aneurysm. In 5th International Conference on Computational and Mathematical Biomedical Engineering-Proceeding (Vol. 1, pp. 172-175).

[21] Bürk, J., Blanke, P., Stankovic, Z., Barker, A., Russe, M., Geiger, J., Frydrychowicz, A., Langer, M. and Markl, M., 2012. Evaluation of 3D blood flow patterns and wall shear stress in the normal and dilated thoracic aorta using flow-sensitive 4D CMR. Journal of cardiovascular magnetic resonance, 14(1), p.80.

[22] Jing, L., Fan, J., Wang, Y., Li, H., Wang, S., Yang, X. and Zhang, Y., 2015. Morphologic and hemodynamic analysis in the patients with multiple intracranial aneurysms: ruptured versus unruptured. PloS one, 10(7), p.e0132494.

[23] Di Achille, P., Tellides, G., Figueroa, C.A. and Humphrey, J.D., 2014. A haemodynamic predictor of intraluminal thrombus formation in abdominal aortic aneurysms. Proceedings of the Royal Society A: Mathematical, Physical and Engineering Sciences, 470(2172), p.20140163.

[24] Ong, C.W., Kabinejadian, F., Xiong, F., Wong, Y.R., Toma, M., Nguyen, Y.N., Chua, K.J., Cui, F.S., Ho, P. and Leo, H., 2019. Pulsatile flow investigation in development of thoracic aortic aneurysm: an in-vitro validated fluid structure interaction analysis. Journal of Applied Fluid Mechanics, 12(6), pp.1855-1872.